We are IntechOpen,
the world's leading publisher of
Open Access books
Built by scientists, for scientists

4,800
Open access books available

122,000
International authors and editors

135M
Downloads

Our authors are among the

154
Countries delivered to

TOP 1%
most cited scientists

12.2%
Contributors from top 500 universities

CLARIVATE ANALYTICS
BOOK CITATION INDEX
INDEXED

WEB OF SCIENCE™

Selection of our books indexed in the Book Citation Index
in Web of Science™ Core Collection (BKCI)

Interested in publishing with us?
Contact book.department@intechopen.com

Numbers displayed above are based on latest data collected.
For more information visit www.intechopen.com

Configuration Proposals for an Optimal Electromagnetic Coupling in Induction Heating Systems

Carrillo, E.
RHI/ BU Glass-Refmex
Mexico

1. Introduction

Induction Heating (IH) is a mature technique for heating metals due it occurs mainly as a consequence of their high electric conductivity. That condition, no necessarily magnetic permeability, enables a suitable electromagnetic coupling that in turns generates intense heat throughput at very high rates at well-defined locations that reduce process cycle time with repeatable quality.

When it comes to induction heating, one must keep in mind that ferromagnetic materials loose their magnetic properties above Curie temperature, thus good electric conductor condition prevails as to be taken into account for a proper work-piece candidate in a IH system, whereas low conducting materials will require high frequency for the excitation coil in order to get the above advantages. Other way to overcome the poor electromagnetic coupling in low conductive work-pieces is by means of assembling a high melting temperature susceptor, which due to its high conductivity heats indirectly the low conductive insert so as to avoid high frequency ancillary equipment thus lowering capital costs.

Despite IH is a well-established heating method; it realizes on empirical rules relating size, frequency and the skin depth of the work-piece to fit a convenient IH scheme.

This chapter is devoted to the development of analytic parameters, which are intended to be taken as guidance to set optimal IH configurations for putting together Inductor and work-piece while the highest electromagnetic coupling is achieved. They should match those optimal conditions that are already known for HI practitioners. The simplest and more ubiquitous geometries dealt in massive induction heating systems happen to be the cylinder and the slab, which are subject matter in this chapter.

Since an IH system can be depicted as a step-down electrical transformer in which the secondary winding is short-circuited and performing as a workpiece, the more intense the influence on the idle excitation coil impedance when the secondary loop is assembled, the greater the occurrence of eddy currents on it. Thus, a proposed reflection coefficient is developed, which is the common factor that precedes both secondary resistance and secondary inductance as appearing in the effective impedance formula for an ideal electrical transformer. The larger the reflection coefficient, the better is the electromagnetic coupling of the workpiece. To undertake that task, a dimensionless treatment of simplified governing differential equation of the eddy current process is given, featuring the shielding parameter

Rω. The above approach has been presented for cylindrical systems (Carrillo, 2008), by considering as boundary values: either a longitudinal or a transverse magnetic flux. In this chapter same treatment also will be given to rectangular workpieces, namely slabs being excited by a transverse flux.

For confronting the proposed model, practical scenarios are taking into account involving the abovementioned workpieces to feed them as an input for computer runs using the commercial FEM software package Quick Field from TERA ANALISYS LTD. Here, the electrical efficiency, or coil efficiency as being the ratio of the power dissipated as heat in the workpiece to the total input power, is referred as a measure of electromagnetic coupling. Results on coil efficiencies confirm the proposed analytical approach.

Furthermore regarding the use of composite loads for improving weakly coupled IH systems as found in susceptor practices, a treatment on a susceptor-insert induction heated device, carried out in Germany (Reichert, 1965) is taken as a reference, for comparing the performance of alternative HI schemes featuring the highest coil efficiency.

Exploring the feasibility of the heating processes other than combustion for both; non-electrical or poor electrical conductors would be an interesting task. Efforts to make more efficient the application of electricity for mass heating would turn it more appealing for Industrial activities, since nowadays environmental issues are becoming constantly stringent, mainly on those related to the Global Warming, hence approaches to reduce green house gas evolving are always welcome.

2. Impedance parameters for an HI system

Eddy currents drive the IH process. The electromagnetic diffusion equations are the governing equations for eddy currents, which are to be solved so as to mathematically model the HI process for a given HI device.

A lumped parameter model is a representation in a mathematical model of a physical system where field variables are simplified down to single scalars. The mathematical analysis of an electrical circuit diagram is much simpler than solving the electromagnetic diffusion equations for the actual HI physical system. Thus impedances, as lumped parameters, are electrically equivalent to those electromagnetic fields distributed in an existing inductor or an element of a circuit. Thereby, magnetic strength and current density distributions for a given HI configuration are to be featured from which basic impedance parameters such as resistances and inductances are stemmed from and then treated in such a way that a reflection coefficient is obtained as a result. In the following a description of how electromagnetic diffusion equations are simplified and set up for being solved, are presented just for cylindrical frames. The same procedure has been carried out using Cartesian coordinates for characterizing the slab geometry.

2.1 Governing equations for featuring eddy currents:
Eddy currents (Krawczyk 1993) occurring in a solid workpiece can be derived by applying Ampere's circuit law for low frequencies, which is:

$$\nabla \times \mathbf{H} = \mathbf{J} \tag{1}$$

The magnetic strength distributions in the workpiece are the solutions of the electromagnetic diffusion equation (Krawczyk 1993), which for rigid bodies is:

$$\nabla^2 \mathbf{H} = \sigma\mu_0 \frac{\partial \mathbf{H}}{\partial t} \tag{2}$$

where, σ (S m^{-1}) is the electric conductivity, μ (V s A^{-1} m^{-1}) is the magnetic permeability of the conductor, t is time (s), $\mathbf{J}$ the current density (A m^{-2}), and $\mathbf{H}$ (A m^{-1}), the magnetic strength field. Components of Eq. (2) are expressed according to the coordinate system suitable to the geometry of the HI configuration. Depending on certain simplifications owing to the symmetry of the excitation source configuration, the components of the magnetic strength vector in Eq. (2) can be uncoupled for the following general cases, namely: an infinitely long conducting cylinder and semi-infinite slab: This consideration usually takes place for neglecting the end and edge effects.

$$\begin{aligned} H_\varphi(z) = cons\tan t, \qquad H_z(\varphi) = constant, \qquad H_r = 0 \qquad & Cylinder \\ H_y = H_z = 0 \qquad\qquad\qquad & Slab \end{aligned} \tag{3}$$

Excitation fluxes are imposed in cylinders by: A solenoidal winding, which impresses an axial magnetic strength on the workpiece and axial coils, which set up an angular magnetic strength inside the workpiece. And for the slab, straight coils, which impose a transverse flux inside the slab, being the coordinate Z for the length, X for the depth and Y for the thickness respectively. Taking into account all the pertinent considerations, the eddy current process will be varying only along the radius for the cylinder and along the thickness "y" for the slab. Furthermore, in the frequency domain, solutions to Eq. (2), are expressed in a general expression as:

$$H_g(\vec{\mathbf{x}}, t) = \left(\operatorname{Re} \hat{H}_g(\ell) + i \operatorname{Im} \hat{H}_g(\ell) \right) \mathbf{exp} i \left(\omega t - p\varphi \right) \tag{4}$$

The position vector $\mathbf{x}$ simplifies to ℓ, which is the coordinate either radius r or thickness y depending on what coordinate system is being considered, ω (s^{-1}) is the electric angular frequency and p is the pair of magnetic poles. Equation (4) is a generic function to be used for solution of Eq. (2), depending on the corresponding subscript g (i.e., Cylindrical φ, z, or Cartesian x), Thus simplified electromagnetic diffusion equations for a given coordinate system then become:

$$\frac{d^2 \hat{H}_\varphi}{dr^2} + \frac{1}{r}\frac{d\hat{H}_\varphi}{dr} - \frac{1+p^2}{r^2}\sigma\mu_0 \hat{H}_\varphi = 0 \tag{5}$$

when the axial coils are performing as an excitation source.

$$\frac{d^2 \hat{H}_z}{dr^2} + \frac{1}{r}\frac{d\hat{H}_z}{dr} - \sigma\mu_0 \hat{H}_z = 0 \tag{6}$$

and Eq. (6) for a solenoidal winding. Finally, for a slab being exposed to the magnetic field from a rectangular cage inductor type, the simplified governing equation becomes:

$$\frac{d^2 \hat{H}_x}{dy^2} + \frac{d\hat{H}_x}{dy} - \sigma\mu_0 \hat{H}_x = 0 \tag{7}$$

2.2 Solution procedure for eddy current equations

The following normalizations for the primitive variables convert Eqs. (5), (6) and (7) into a pair of dimensionless coupled equations.

i) The dimensionless length χ, defined as either the ratio of the outer radius R to any inner radius r for the cylinder, and the ratio of slab thickness Y to any distance along the "y" coordinate:

$$\chi = \frac{r}{R}, \quad . \quad \chi = \frac{y}{Y} \tag{8}$$

R or Y might be referred as the work-piece characteristic length as used in the principle of similitude technique.

ii) The electromagnetic variables are normalized to the difference between the real parts of the magnetic strength at the surface and at the axis. The magnetic strength subscript g takes labels of φ, z, or y, according to the configuration being analyzed. Since there is no magnetic field at the workpiece axis owing to the magnetic shielding process, then Re H_g (ℓ =0) and Im H_g (ℓ =0) are equal to zero. Thus, news dimensionless magnetic variables turn out as:

$$\Theta_g = \frac{\operatorname{Re} \hat{H}_g(\ell)}{\operatorname{Re} \hat{H}_g(surface)} . \tag{9}$$

$$\Psi_g = \frac{\operatorname{Im} \hat{H}_g(\ell)}{\operatorname{Re} \hat{H}_g(surface)} . \tag{10}$$

The electromagnetic properties of the material are gathered in the dimensionless number $R\omega$ termed the screen or shielding parameter, which relates the ability of a conducting medium to exclude high-frequency magnetic fields from its core:

$$R\omega_{cylinder} = \sigma\mu\omega R^2, \qquad R\omega_{slab} = \sigma\mu\omega Y^2 . \tag{11}$$

$R\omega$ also can be expressed in term of the electromagnetic skin depth δ, being $\delta = \sqrt{(2/\omega\sigma\mu)}$

$$R\omega_{cylinder} = 2\left(\frac{R}{\delta}\right)^2, \qquad R\omega_{slab} = 2\left(\frac{Y}{\delta}\right)^2 . \tag{12}$$

in terms of the workpiece thickness,

$$\frac{D}{\delta} = \sqrt{2R\omega_{\text{cylinder}}}, \qquad \frac{Y}{\delta} = \sqrt{2R\omega_{\text{slab}}} . \tag{13}$$

Following the procedure for solving the simplified governing equation for the dimensionless angular magnetic fields is given. Same treatment is to be given for the remaining cases dealt so far. By substituting Eqs. (9), (10), and (11) into Eq. (5), a set of simultaneous ordinary equations for both the real and imaginary parts of the dimensionless angular magnetic is built:

$$\frac{d^2\Theta_\varphi}{d\chi^2} + \frac{1}{\chi}\frac{d\Theta_\varphi}{d\chi} - \left(\frac{1+p^2}{\chi^2}\right)\Theta_\varphi + (R\omega)\Psi_\varphi = 0 \tag{14}$$

$$\frac{d^2\Psi_\varphi}{d\chi^2} + \frac{1}{\chi}\frac{d\Psi_\varphi}{d\chi} - \left(\frac{1+p^2}{\chi^2}\right)\Psi_\varphi - (R\omega)\Theta_\varphi = 0 \tag{15}$$

With regard to the complex plane, real zero is set equal to the right-hand terms of Eqs. (14) and (15). The systems of coupled equations are solved by means of the Newton shooting method (Constantinides, 1987) with the following labels: The boundary values for the magnetic fields at the axis are fixed to zero to resemble the cancellation of fields at that point:

$$\left.\frac{d\Theta_g}{d\chi}\right|_{\chi=0} = y_1(y_4 = 0) = 0 \tag{16}$$

$$\left.\frac{d\Psi_g}{d\chi}\right|_{\chi=0} = y_2(y_4 = 0) = 0 \tag{17}$$

$$\left.\Psi_g\right|_{\chi=0} = y_3(y_4 = 0) = 0 \tag{18}$$

The value of y_4 at the left boundary is assumed to be nearly zero, e.g. 10^{-8}, to avoid singularities. The real magnetic strength is set to unity at the cylinder surface:

$$\left.\Theta_g\right|_{\chi=1} = y_5(y_4 = 1) = 1 = \frac{H_g}{H_g} \tag{19}$$

The missing initial condition is the left-boundary value y_5, which cannot be set because the right-boundary value has already been granted. Therefore, this missing initial condition is estimated by means of an initial shoot γ_5, keeping the notion of magnetic shielding, as required by Lenz's Law:

$$\left.\Theta_g\right|_{\chi=0} = y_5(y_4 = 0) \approx \gamma_5 \approx 0 \tag{20}$$

The field should fade toward the axis. The Newton shooting procedure is balanced by a variational equation set, which weights the certainty of the guessed shoot γ.

$$y_6 = \frac{d}{d\chi}\left(\frac{\partial\Theta_g}{\partial\gamma_5}\right) = \frac{\partial y_1}{\partial\gamma_5}, \quad y_7 = \frac{d}{d\chi}\left(\frac{\partial\Psi_g}{\partial\gamma_5}\right) = \frac{\partial y_2}{\partial\gamma_5},$$

$$y_8 = \frac{\partial\Psi_g}{\partial\gamma_5} = \frac{\partial y_3}{\partial\gamma_5}, \qquad y_9 = \frac{\partial\chi}{\partial\gamma_5} = \frac{\partial y_4}{\partial\gamma_5}, \tag{21}$$

$$y_{10} = \frac{\partial\Theta_g}{\partial\gamma_5} = \frac{\partial y_5}{\partial\gamma_5}$$

The error to converge the solution is less than 10^{-8}.

2.3 Approaching of an HI system as a short-circuited electric transformer

An induction heating system can be depicted as a step-down electrical transformer in which the secondary winding is short-circuited. The secondary winding performs as a workpiece in which ohmic heat is dissipated due to an induced electric field.

2.3.1 Circuit equations

The initial approach to feature an electric transformer is carried out by analyzing the following coupled differential equations

$$V_0 = R_c \frac{\mathrm{d}I_c}{\mathrm{d}t} + L_c \frac{\mathrm{d}I_c}{\mathrm{d}t} + M \frac{\mathrm{d}I_w}{\mathrm{d}t}$$
$$0 = R_w \frac{\mathrm{d}I_w}{\mathrm{d}t} + L_w \frac{\mathrm{d}I_w}{\mathrm{d}t} + M \frac{\mathrm{d}I_c}{\mathrm{d}t} \tag{22}$$

The variables are the electric current I (A), electrical resistance R (Ω), and self-inductance L (H). The mutual inductance M (H) is common to both loops. The primary circuit with excitation voltage V_0 is denoted using subscript c and the corresponding secondary circuit, as featured by the eddy current pattern inside the workpiece, is labeled with subscript w. We assume that the voltages and currents are harmonic variables:

$$V_0 = \hat{V}_0 \, \mathrm{e}^{\mathrm{i}\omega t}$$
$$I_c = \hat{I}_c \, \mathrm{e}^{\mathrm{i}\omega t} \tag{23}$$

where a hat (^) on top of variables denotes a complex phasor and i represents the complex number $\sqrt{(-1)}$. Then, by substituting Eqs (23) into Eq. (22) and some rearrangement, the effective impedance Z can be obtained:

$$\hat{Z} = \left(R_c + \frac{\omega^2 M^2}{R_w^2 + \omega^2 L_w^2} R_w \right) + \mathrm{i} \cdot \left(\omega L_c - \frac{\omega^2 M^2}{R_w^2 + \omega^2 L_w^2} \omega L_w \right) \tag{24}$$

Equation (24) shows that the load is electrically equivalent to a resistance and a negative inductance placed in the primary circuit. The common factor that precedes both secondary resistance and secondary inductance might be envisaged as a reflection coefficient for the excitation circuit:

$$\text{reflection coefficient} \equiv \frac{\omega^2 M^2}{R_w^2 + \omega^2 L_w^2} \tag{25}$$

The larger the reflection coefficient, the better is the electromagnetic coupling of the workpiece. Hence, the optimization process consists of identifying conditions under which the reflection coefficient is enhanced.

2.3.2 Impedance parameters

The resistive and inductive load of a HI system can be derived from the balance of energy inside an electromagnetic field, as described by Poynting (Krawczyk 1993) as follows:

$$\oint_A \left(\hat{\mathbf{E}} \times \hat{\mathbf{H}}\right) \bullet \mathbf{n} \, dA = -i \cdot 2\omega\mu_0 \int_V \tfrac{1}{4}\left|\hat{\mathbf{H}}\right|^2 dV - \int_V \tfrac{1}{2}\left|\hat{\mathbf{J}}\right|^2 dV \tag{26}$$

Equation (26) comprises the vectors **B**, the induction flux (V s m^{-2}), **E**, the electric field (V m^{-1}), **J**, the current density (A m^{-2}), and **H** (A m^{-1}), the magnetic strength field. The terms within parentheses are the complex modules of the corresponding variables.

The workpiece resistance R_w is taken from the second term on the right-hand side of Eq. (26), the real part of the influx of the Poynting vector:

$$R_w = \frac{1}{\sigma_w \left(I_w\right)^2} \iiint \tfrac{1}{2}\left|\hat{J}_w\right|^2 \cdot dz \cdot d\varphi \cdot r dr \tag{27}$$

The dummy variables for the integral in Eq. (27) are expressed in cylindrical coordinates. Let us assume that

$$I_w = N_c I_c \tag{28}$$

since the secondary loop is equivalent to a one-turn coil as an idealized transformer. Here N_c is the number of coil turns in the excitation winding. By substituting Eq. (28) into Eq. (27) and integrating for angular and axial coordinates, this yields:

$$R_w = \frac{\pi}{\sigma_w} \frac{Z_\infty}{N_c^2 I_c^2} \cdot \int_0^R \left|\hat{J}_w\right|^2 \cdot r dr \tag{29}$$

The upper limit R in the integral is the outer radius of the workpiece, and Z_∞ represents the length of an infinitely long cylinder. The workpiece inductance L_w stems from the first term on the right-hand side of Eq. (26), which represents the magnetic energy stored in that volume.

$$L_w = \frac{\mu_0}{\left(I_w\right)^2} \iiint \tfrac{1}{2}\left|\hat{H}_w\right|^2 \cdot dz \cdot d\varphi \cdot r dr \tag{30}$$

Similarly, by substituting Eq. (28) into Eq. (30), the workpiece inductance can be expressed as:

$$L_w = \omega\mu_0\pi \frac{Z_\infty}{N_c^2 I_c^2} \cdot \int_0^R \left|\hat{H}_w\right|^2 \cdot r dr \tag{31}$$

In addition, the mutual inductance M can be derived from the expression for the magnetic energy stored in the space shared by the excitation coil and the workpiece, as follows:

$$M = \frac{1}{I_c I_w} \iiint \left(\mathbf{H}_c \bullet \mu_0 \mathbf{H}_w\right) \cdot dz \cdot d\varphi \cdot r dr \tag{32}$$

Assuming harmonic behavior for the electromagnetic variables, Eq. (32) can be expressed as:

$$M = \frac{\mu_0}{I_c I_w} \iiint \tfrac{1}{2}\text{Re}\left(\hat{H}_c \cdot \hat{H}_w^*\right) \cdot dz \cdot d\varphi \cdot r dr \tag{33}$$

The superscript (*) for H_w represents its complex conjugate. Thus, by substituting Eq. (28) into Eq. (33) and integrating for axial and angular coordinates yields:

$$M = \frac{Z_\infty \mu_0 \pi}{N_c I_c^2} \int_0^R \left(\text{Re}\,\hat{H}_c \,\text{Re}\,\hat{H}_w + \text{Im}\,\hat{H}_c \,\text{Im}\,\hat{H}_w \right) \cdot r \, dr \tag{34}$$

Thus, by substituting Eqs. (29), (31) and (34) into Eq. (25), the reflection coefficient can be expressed as:

$$\frac{\omega^2 M^2}{\left(R_w^2 + \omega^2 L_w^2 \right)} = N_c^2 \frac{\omega^2 \mu_0^2 \left[\int_0^R \left(\text{Re}\,\hat{H}_c \,\text{Re}\,\hat{H}_w + \text{Im}\,\hat{H}_c \,\text{Im}\,\hat{H}_w \right) \cdot r \, dr \right]^2}{\left[\frac{1}{\sigma_w^2} \left(\int_0^R \left| \hat{J}_w \right|^2 \cdot r \, dr \right)^2 + \omega^2 \mu_0^2 \left(\int_0^R \left| \hat{H}_w \right|^2 \cdot r \, dr \right)^2 \right]} \tag{35}$$

Multiplying both the numerator and denominator in Eq. (35) by $R^4 \sigma_w^2$ yields:

$$\frac{1}{N_c^2} \frac{\omega^2 M^2}{\left(R_w^2 + \omega^2 L_w^2 \right)} = \frac{\sigma_w^2 \omega^2 \mu_0^2 R^4 \left[\int_0^R \left(\text{Re}\,\hat{H}_c \,\text{Re}\,\hat{H}_w + \text{Im}\,\hat{H}_c \,\text{Im}\,\hat{H}_w \right) \cdot r \, dr \right]^2}{R^4 \left(\int_0^R \left| \hat{J}_w \right|^2 \cdot r \, dr \right)^2 + \sigma_w^2 \omega^2 \mu_0^2 R^4 \left(\int_0^R \left| \hat{H}_w \right|^2 \cdot r \, dr \right)^2} \tag{36}$$

This expression describes the reflection coefficient in terms of fundamental electromagnetic variables such as the magnetic strength and current density.

2.3.3 Dimensionless reflection coefficient

The reflection coefficient represents a measure of the coupling of the induced electromagnetic field to the excitation source. Therefore, the electromagnetic parameters that result in a maximum reflection coefficient while keeping minimal either the operational frequency or workpiece size for a given induction heating design need to be identified. For generalization, the task involves searching for the lowest shielding parameter $R\omega$ that matches the highest reflection coefficient.

Variables in the reflection coefficient, such as the dimensions, the electromagnetic properties of the workpiece and the excitation frequency, can be expressed in terms of shielding parameter $R\omega$ by substituting Eq. (11) into Eq. (36), resulting in:

$$\frac{1}{N_c^2} \frac{\omega^2 M^2}{\left(R_w^2 + \omega^2 L_w^2 \right)} = \frac{\left(R\omega \right)^2 \left[\int_0^R \left(\text{Re}\,\hat{H}_{c,g} \,\text{Re}\,\hat{H}_{w,g} + \text{Im}\,\hat{H}_{c,g} \,\text{Im}\,\hat{H}_{w,g} \right) \cdot r \, dr \right]^2}{R^4 \left[\int_0^R \left| \hat{J}_{w,g} \right|^2 \cdot r \, dr \right]^2 + \left(R\omega \right)^2 \left[\int_0^R \left| \hat{H}_{w,g} \right|^2 \cdot r \, dr \right]^2} \tag{37}$$

Therefore, the procedure to be followed comprises finding both the magnetic strength and the current density distributions inside the workpiece that match the minimum shielding parameter $R\omega$, which maximizes the reflection coefficient, as shown in Eq. (37).

As required by the similarity criteria for scaled process analysis, the terms inside the square brackets in Eq. (37) are dimensionless variables, and hence they are defined as follows. The dimensionless complex magnetic strength is

$$\Xi_g = \Theta_g + i\Psi_g \tag{38}$$

and the relationship between the time-averaged value of Ξ with its complex module is

$$\overline{\Xi_g^2} = \tfrac{1}{2}\mathrm{Re}\left(\Xi_g \cdot \Xi_g^*\right) = \frac{\left|\Xi_g\right|^2}{2} \tag{39}$$

Similarly expressions for the dimensionless current densities Γ_g, are obtained by developing Ξ with components Θ_g and Ψ, following the Ampere Law while holding the corresponding dimensionless conditions. Then time-averaged dimensionless axial current density is obtained:

$$\frac{\left|\Gamma_z\right|^2}{2} = \frac{1}{2}\left(\left(\frac{d\Theta_\varphi}{d\chi} + \frac{\Theta_\varphi}{\chi}\right)^2 + \left(\frac{d\Psi_\varphi}{d\chi} + \frac{\Psi_\varphi}{\chi}\right)^2\right) \tag{40}$$

The scalar component of Γ_r has been neglected for simplicity. The expressions in Eq. (39), and (40) are then substituted in Eq. (37). The outer radius assigned as the upper limit in the integrals is set to unity, in accordance with Eq. (8)

$$\frac{1}{N_c^2}\left(\frac{\omega^2 M^2}{R_w^2 + \omega^2 L_w^2}\right)_{\text{dimensionless}} = \frac{\left[\int_0^1 \left(\Theta_{c,g}\Theta_{w,g} + \Psi_{c,g}\Psi_{w,g}\right)\cdot\chi d\chi\right]^2}{\dfrac{1}{(R\omega)^2}\left(\int_0^1 \left|\Gamma_{w,g}\right|^2\cdot\chi d\chi r\right)^2 + \left(\int_0^1 \left|\Xi_{w,g}\right|^2\cdot\chi d\chi\right)^2} \tag{41}$$

The dimensionless excitation magnetic strength $\Xi_{c,g}$ is taken as a constant through the linked flux and its complex module is assumed to equal 1. Under ideal conditions, since the coil is non-ferrous, there will be a $\pi/4$ phase shift inside the imposed field $\Xi_{c,g}$, and hence it dissembles into its real and imaginary parts as follows:

$$\hat{\Xi}_{c,g} = \Theta_{c,g}\frac{\sqrt{2}}{2} + i\Psi_{c,g}\frac{\sqrt{2}}{2} \tag{42}$$

In addition, the gap between the workpiece and the excitation coil is assumed to be negligible, so the value of the magnetic strength in the excitation coil is considered to be the same as the real magnetic strength at the workpiece surface, which was taken as a normalizing value:

$$\Theta_{w,g} = 1 = \Theta_{c,g} = \Psi_{c,g} \tag{43}$$

Thus, Eq. (42) is transformed to:

$$\hat{\Xi}_{c,g} = \frac{\sqrt{2}}{2}\left(1 + i\right) \tag{44}$$

By substituting Eq. (44) into Eq. (41), the expression for the dimensionless reflection coefficient becomes for the cylindrical workpiece:

$$\frac{1}{N_c^2}\left(\frac{\omega^2 M^2}{R_w^2 + \omega^2 L_w^2}\right)_{\text{dimensionless}} = \frac{\dfrac{\sqrt{2}}{2}\left[\displaystyle\int_0^1\left(\Theta_{w,g} + \Psi_{w,g}\right)\cdot\chi\,\mathrm{d}\chi\right]^2}{\dfrac{1}{(R\omega)^2}\left(\displaystyle\int_0^1\left|\Gamma_{w,g}\right|^2\cdot\chi\,\mathrm{d}\chi\right)^2 + \left(\displaystyle\int_0^1\left|\Xi_{w,g}\right|^2\cdot\chi\,\mathrm{d}\chi\right)^2} \qquad (45)$$

whereas for the slab, taking into account the Cartesian variable is: $v = y/Y$ then the expression for its reflection coefficient is:

$$\frac{1}{N_c^2}\left(\frac{\omega^2 M^2}{R_w^2 + \omega^2 L_w^2}\right)_{\text{dimensionless}} = \frac{\dfrac{\sqrt{2}}{2}\left[\displaystyle\int_0^1\left(\Theta_{w,\text{cage}} + \Psi_{w,\text{cage}}\right)\cdot\mathrm{d}v\right]^2}{\dfrac{1}{(R\omega)^2}\left(\displaystyle\int_0^1\left|\Gamma_{w,\text{cage}}\right|^2\cdot\mathrm{d}v\right)^2 + \left(\displaystyle\int_0^1\left|\Xi_{w,\text{cage}}\right|^2\cdot\mathrm{d}v\right)^2} \qquad (46)$$

3. Analysis on electromagnetic coupling

In this section some numerical results stemmed from the previous analytical assessment on optimal conditions where electromagnetic coupling occurs in several HI systems are presented and some of them confronted to those already known by IH practitioners.

Thereby, for obtaining reflection coefficients for cylindrical and rectangular workpieces when exposed to either longitudinal or transverse excitation fluxes, whatever the case is selected, values of the shielding parameter $R\omega$ are to be varied and fed as an input for the dimensionless electromagnetic diffusion equations, thus dimensionless magnetic strength and current density distributions are calculated and integrated and then treated as in Eq (43) or Eq. (44) whichever is proper.

Fig.1 gathers various reflection coefficients as dependant of the shielding parameter.

Fig. 2 shows same coefficients but now as a function of the ratio of the workpiece thickness to skin depth, which is more familiar to HI practitioners.

The relationship between shielding parameter and skin depth is regarded in Eq. (36). Reflection coefficent, hence electromagnetic coupling, seems to enhance in workpieces subjected to excitation transverse flux as the size decreases being the slab the shape that dissipates more power while either minimum frequency is applied or the smallest size is employed.

Nevertheless, the reflection coefficient for slabs is of the order of 10-4 so it is displayed in the right-hand side ordinate of Figs. 1 and 2 as multiplied by the square of 100 coil turns, which might mean when heating a slab, a multilayer inductor should be used in order to have proper electromagnetic coupling.

For longitudinal flux applications, the reflection coefficient is the highest for the workpiece diameter /skin depth at 5.7. This ratio together with the range of the width of the "bell" of the corresponding curve, which goes from 4.7 to 6.25, matches what is stated by Rudnev (Rudnev et al., 2003) There, a rule of thumb is referred which stipulates current cancelation, hence no induction heating, will take place if the ratio of workpiece diameter to current
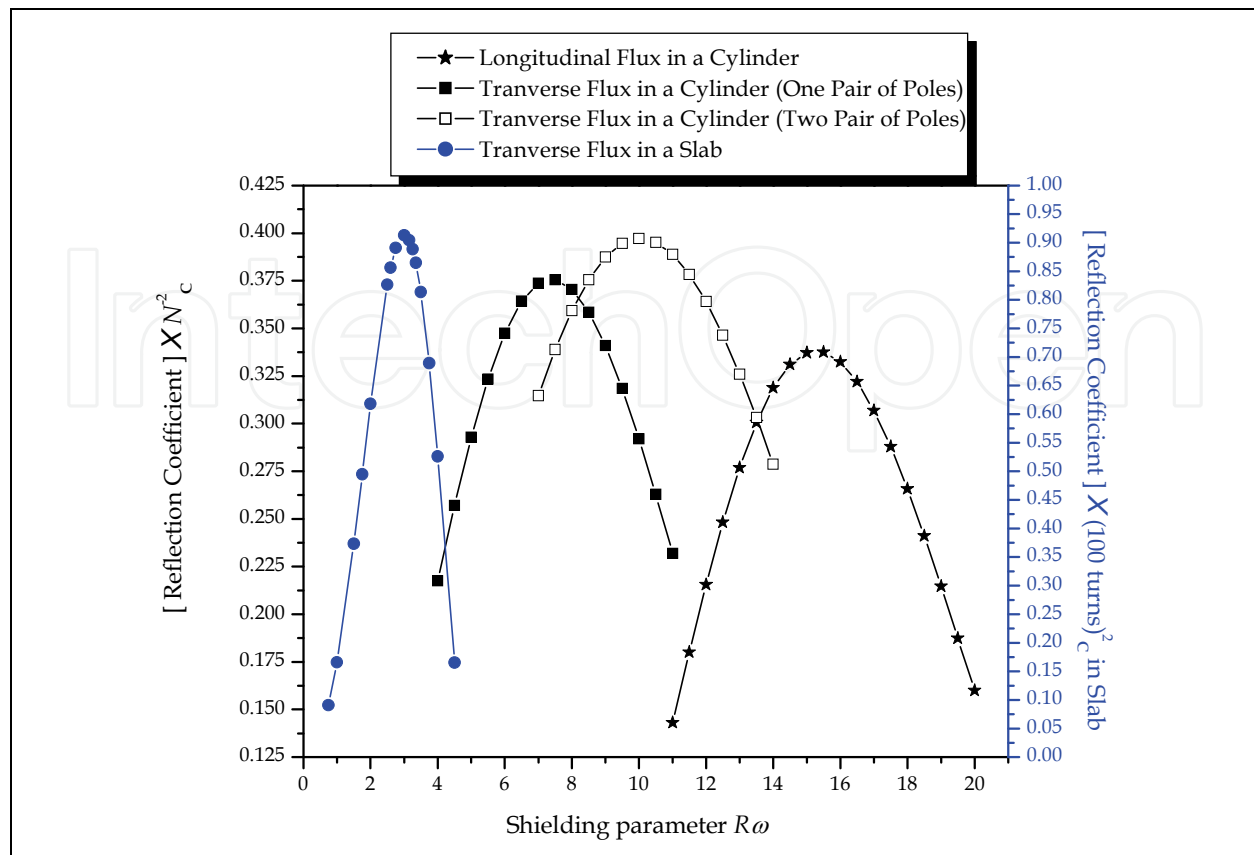
Fig. 1. Influence of the Excitation Coil Configuration on Electromagnetic Coupling in HI Systems, as a Function of Shielding Parameter.

penetration depth is less than four. Beyond of ratio 6 it will only slightly increase the heating induction efficiency.

Simpson (Davies & Simpson,1979) tried to find analytically those optimal conditions by invoking the Bessel functions ber and bei from which a maximum p parameter should have been associated to above mentioned workpiece diameter to skin depth ratios, actually resulting in ratios lower than those found in practice. Nevertheless, it is close to the range where the cylindrical devices excited by one-pair of poles transverse flux achieve their maximum reflection coefficients as it can be seen in Fig.2.

For a single phase device, the one-pair-of-poles windings would need the full 180 ° arc in each hemisfere of the cylinder to accomodate the excitation coils, thus the HI process would be affected by the so called proximity effect due to the closeness of the ends of the coils carrying opposite currents. A resource to maintain far enough the coils could be placing the excitation coils half way the full arc of the hemisphere in such a manner that the whole circumference is divided in four parts having the same length: two parts opposing each other as the locus for the windings and the other section 90° apart to give room and avoid the proximity effect. See Figs. 6 b) and 11 a). This layout is equivalent to two-pair-of-poles windings whose configuration also is analysed and reflection coefficient plotted in Figs. 1 and 2. This arrangement seems to be more practical hence it is considered for further Finite Element Software simulations. The range where higher shielding parameters occur lies between those corresponding to one-pair of poles and solenoidal configurations. It shows the highest reflection coefficient among the analysed configurations.
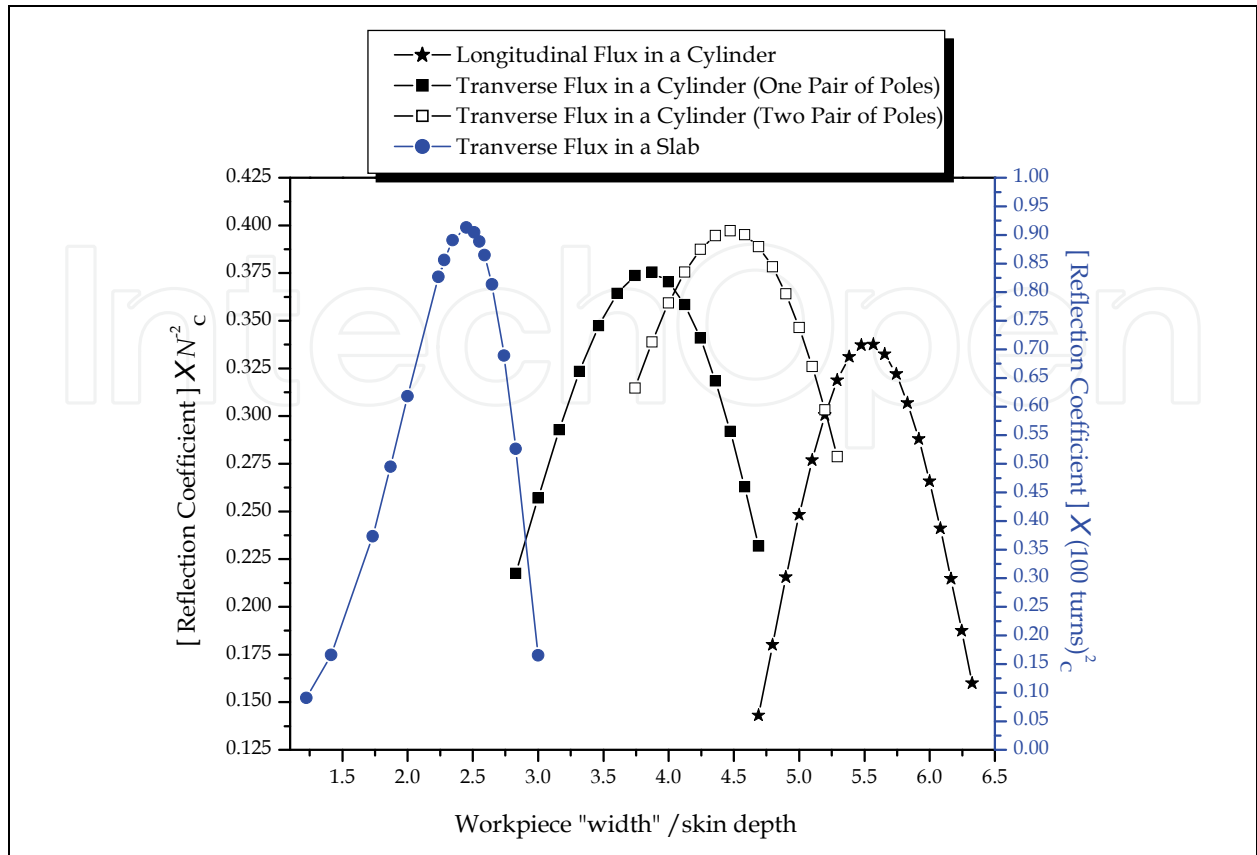
Fig. 2. Influence of the Excitation Coil Configuration on Electromagnetic Coupling in HI Systems, as a Function of the Ratio of Workpiece Width to Skin Depth.
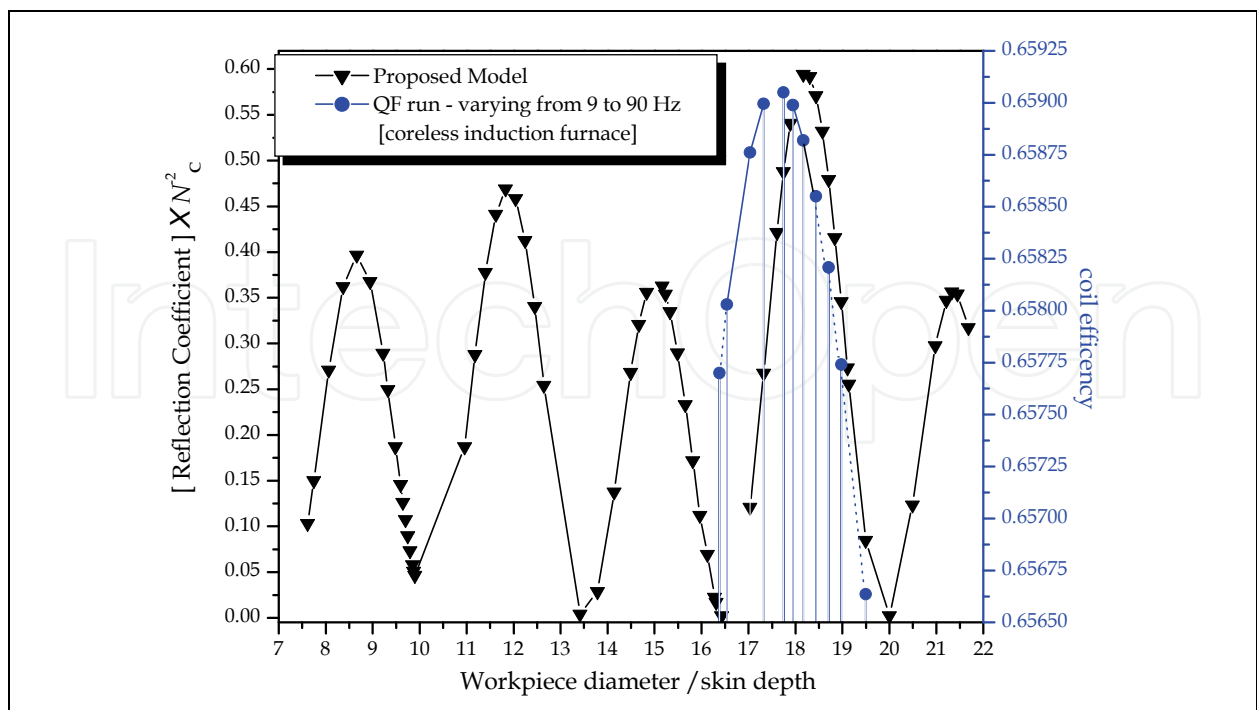

Fig. 3. Electromagnetic Coupling Performance at Higher Shielding Parameters for a Solenoid Coil Configuration

On the other hand, Fig. 2 shows the lowest workpiece diameter to skin depth ratio range for solenoidal coil configurations, e.g. longitudinal flux applications, where a mininum either frequency or HI device size can be fixed while keeping high electromagnetic coupling, thus high efficiency in the energy conversion. Nevertheless, there are also industrial applications such as metal melting when using mains frequency coreless induction furnaces whose sizes are above that optimal range and performig with relatively high efficiencies. That problem was tackled in Germany at the end of the 1950's (Davies & Simpson, 1979). The proposed reflection coefficient also could explain that break through, since those obtained at higher shielding parameters seems to have cyclic behaviour resulting in waves of maximums and minimums depending on the value of a given workpiece to skin depth ratio, see Fig. 3.

The range shielding parameters corresponding to the highest reflection coefficients has been chosen and compared to certain computed coil efficiencies, which will be discussed in further section.

3.1 Coil efficiency as a means of measuring of electromagnetic coupling in HI systems

Since being the reflection coefficient an analytical concept difficult to be measured, if not impossible, indirect parameters that are enhanced when eddy currents occur in the workpiece have to be found for comparison. There exists a practical index that relates the electromagnetic coupling of a HI assemblage, namely the electric efficiency or coil efficiency defined as the fraction of the total energy that takes into account only the ohmic losses released in the workpiece. The later is more commonly known and it will be referred from now on. Therefore parameters of interest would be: the overall Ohmic losses for the global HI system, e.g. those occurring in the inductor coil and workpiece, and the heat released solely in the work piece as well. Then, the expression for the coil efficiency, η_c, becomes:

$$\text{Coil efficiency} \equiv \frac{\text{Ohmic losses in workpiece}}{\text{Total Losses}} = \eta_c \qquad (47)$$

4. Simulating of coil efficiencies for single HI assemblages

In this section the calculation of coil efficiencies is undertaken for mains frequency HI schemes considering several inductor configurations for massive slabs and billets, these as a solid workpieces made out of an aluminium alloy having 2.32×10^7 [S m^{-1}] of electric conductivity and a thermal insulation gap of 0.001 [m] . Those scenarios have been modelled using the 2D Finite Element software QUICK FIELD 5.7 from TERA ANALYSIS LTD, which will be referred as QF from now on. All of the exercises were carried out in the high precision mode.

Table 1 shows parameters whose reflection coefficients at 60 Hz are the highest on each of the three schemes dealt so far. From there, corresponding dimensions as in 6th and 7th rows have been taken as an input for the QF software for obtaining the joule heat developed in inductor and workpiece hence the coil efficiency for a short range of frequencies around 60 Hz.

4.1 Multilayer inductor configurations

When dealing with mains frequency in HI systems, the increase of number of coil turns has to be taken into account so as to avoid high amperage in the excitation coil due to the low impedance driven by very low frequencies. The total current then is uniformly distributed

Excitation Magnetic Flux Application	Longitudinal	Transverse	Transverse
Inductor Configuration	Solenoidal	One Pair of Poles	Rectangular Cage
Shielding Parameter $R\omega$	15.5	7.75	3
Workpiece "Thickness"/ skin depth	5.55	3.75	2.45
Workpiece Geometry	Cylinder	Cylinder	Slab
Workpiece „Thickness"	0.0751 m	0.0531 m	0.0313 X 0.358 width
Workpiece length	0.36 m	0.2555 m	0.306 m
Inductor-workpiece Insulation gap	0.0121 m	0.0121 m	0.0121 m

Table 1. Parameters for an Optimal Electromagnetic Coupling at 60 Hz for Solid Aluminium

over the whole radial depth of the winding. Too many turns imply small conductors, hence, small water passages, giving the risk of clogging, when windings are made from hollow water-cooled copper. In addition, by using multiple layers of tubular coils, outer layers, those further away from the workpiece, heat inner layers as well as the workpiece, worsening that way coil efficiency. Therefore, multilayer does not allow the use of internally cooled conductors. Furthermore, multi-layers are suitable if the conductors are thin compared with the skin depth.

To overcome the above shortcomings, recourse is made for applying external cooling to the winding, (Harvey, 1977) where coolant is forced to circulate trough spacing between bunchs of individual conductors as follows:

a. Axial cooling.- Radial gaps separate turns of each layer, whereby coolant flows over the interlayer room as it is directed axially through the winding. See Fig. 4 a).

b. Edge cooling.- The coil comprises several stacks of tight layers forming a disc wrapped around and twisting itself into a spring in such a manner that a gap is allowed between each stack. Coolant is caused to flow in the gap, and radially guided in a sinuously fashion. That disc becomes a plate for the Slab /Cage-shaped inductor configuration. See Fig 4 b).

The two of the multilayer coil arrangements are simulated for the longitudinal flux case, e.g. solenoidal inductor configuration whereas the edge cooling arrangement is simulated just for the Transverse Flux cases, namely: Two-pair of poles and rectangular cage configurations. In all cases the pitch coil is neglected for simplification.

4.3 HI design data for quick field software input

Table 2 shows the dimension and number of turns that were fed to the QF runs for the configurations that were dealt so far. Current source was fixed to 150 [A] for all the cases. The section of the coil is 4.1 mm X 7 mm. The Inductor-Workpiece gap was considered the same for all the exercises. It is assumed from a practical point of view, a given constant thickness for covering thermal insulation issues is needed to withstand same levels of high

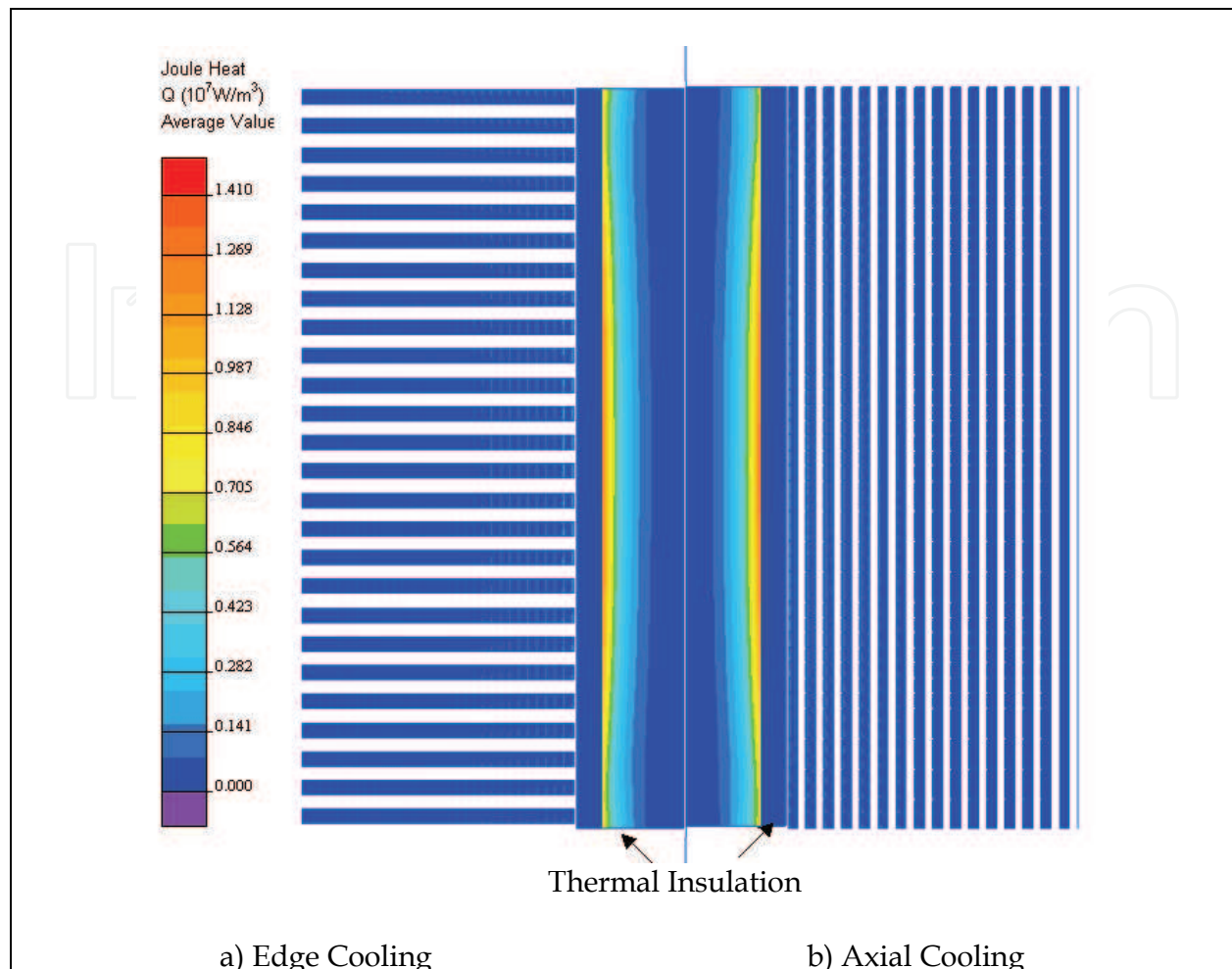| Inductor Type	Edge Cooling	Axial Cooling	One Pair of Poles	Rectangular Cage
Excitation Flux	Longitudinal	Longitudinal	Transverse	Transverse
Layers	30	16	30	30
Stack of Coils	26	49	11 each side	26 each side
Turns	780	784	330	780

Table 2. HI layout input parameters for QF simulations

Fig. 4. Layout of Multilayered Coil excited by Longitudal Flux. Left hand Side: Half Section of an Edge Cooled Inductor. Right Hand Side: Half Section of an Axial Cooled Inductor

power density dissipation no matter the workpiece size, despite the smaller sizes as for the slab and the pole paired transverse flux cases, would call for a gap size proportional to corresponding workpiece sizes so as to have a fair comparison. The layout for each case can in Figs: 4 a), 4 b), 6 b) and 6 a) respectively.

4.4 Multilayered coil schemes powered by a longitudinal excitation flux
In Fig. 4 the Joule heat distribution in each half of the longitudinal section for the above cases have been put together as QF displayed results. The left-hand-side shows the edge cooled multilayered coil whereas the right hand side does axial cooled multilayered coil. Coolant impingement aims 90° when it is compared each other: Towards the gap between wounded discs for the former whereas towards the interlayer gap for the later. Both coils are externally cooled.

Fig. 5 shows the electromagnetic coupling parameter for two solenoidal multilayered schemes both with almost same number of coils, eg, 784 for axial cooling configuration and 780 for edge cooling configuration. The former shows slightly better coil efficiency than later and both of them matches the locus where the maximum reflection coefficient is predicted to occur.
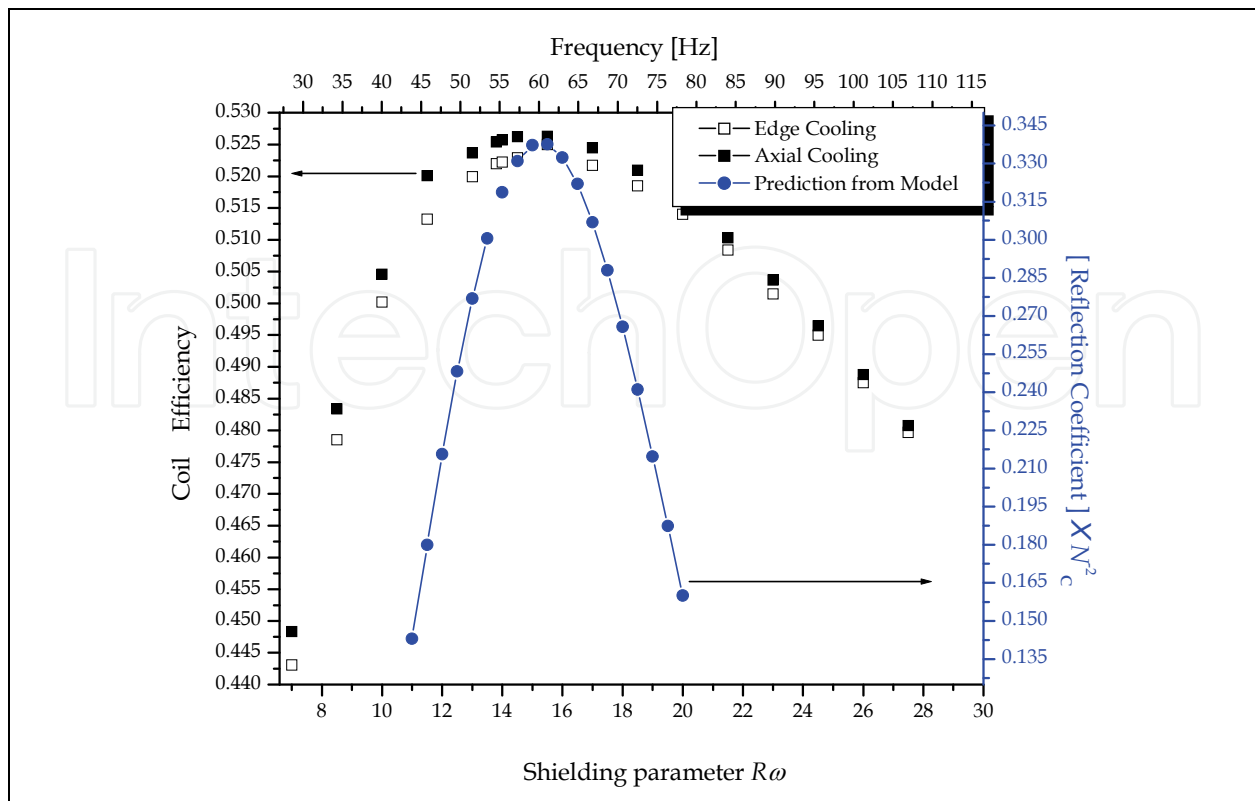
Fig. 5. Electromagnetic Coupling Parameter Performance in Longitudinal Flux Schemes

4.5 Multilayered coil scheme powered by one one–pair-of poles excitation transverse flux

In Fig. 6 b) shows the transverse section of a cylinder being heated by means of an inductor wounded in such a manner that it looks shaped as a star from a top view. Current is directed towards inside the plane in the top half whereas current is going outside the plane in the bottom half and it goes alternatively according to frequency. The coolant is caused to flow along the edges of the branches of the star. Broad spaces between branches make easier the cooling that is carried out externally on the inductor. Straight coils of each half of the inductor might be connected each other at the ends with radial coils in a progressive "rotating X" pattern for the blind side and for the opposite side, where the workpiece might be inserted, circular coils as in windings at the ends of an induction motor stator.

The cylinder radius was chosen 0.052 m as the minimum size for maximum reflection coefficient for a one –pair- of poles transverse excitation flux. Both coil efficiency and one pole pair flux configuration reflection coefficient curves develop the same slope at lower shielding parameters. Nevertheless the maximum coil efficiency and reflection coefficient occur at shielding parameter $R\omega = 10$, but now for the two-pair of poles configuration. By looking the regions at both sides, it can be seen that room for an extra pair of poles can be accommodated in that place. Thereby, the reflection coefficient modeled for two-pair of poles configuration can be approached to the presented example by appealing geometry considerations. As a drawback of this configuration, concentrated Joule heat dissipation may be located near to the centres of each winding, leaving a "cold spot" at right angles from them, which are located at the left-hand side and at the right-hand side of the Fig 6 b). In order to spread the released power, a rotating mechanism fixed to one end of the billet

would enable to expose all the surface of a solid workpiece to a uniform excitation transverse flux. Another alternative is to fix an inductor similar to a stator of a one-pair-of poles tri-phase induction motor for setting a travelling transverse excitation flux, so as to avoid the formation of uneven-heated regions in the workpiece.
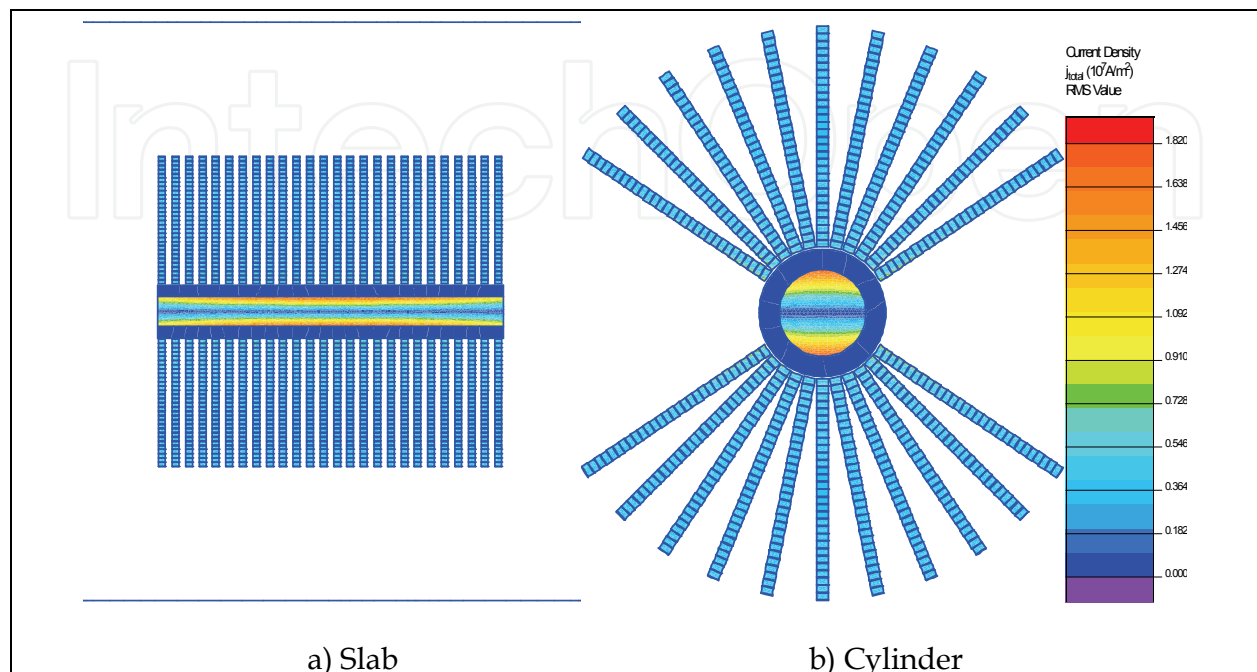

Fig. 6. Top View of Layouts of Multilayered Coil excited by Transverse Flux. Left hand Side: Rectangular Cage Inductor. Right Hand Side: Star Inductor.

4.6 Multilayered rectangular coil scheme powered by a transverse excitation fFlux

Fig. 6 a) shows the transverse section of a solid slab being heated by means of an inductor where plates of piled coils are separated to allow room for the coolant. Since this configuration is being excited by a transverse flux, current circulates aiming inside the plane in the top half whereas current leaves outside the plane in the bottom half in an alternated fashion according to frequency. Fig. 8 shows that the maximum coil efficiency is achieved at $R\omega = 3$ which corresponds to a slab thickness to skin depth ratio of 2.45, see Eq. (12), which matches the well-known practical rule for heating inductively slabs. Both coil efficiency and reflection coefficient start to decay beyond $R\omega = 3$. The former decays slowly whereas the later decays abruptly.

5. Simulating of coil efficiencies for HI susceptor assemblies

The suceptor is generally a relatively good electrically conductive insert possessing high melting point, which is assembled together with the material to be heated, so as to the later is heated indirectly by the following heat transfer modes: conduction and radiation. This is the main use for susceptors. It is required due to the poor electromagnetic coupling of electrically low conductors, unless high frequency is used. The aim here is to improve energy conversion efficiency. With the same purpose, susceptors are also used for the heating of very-good conductors such as aluminium and copper, since it is well-known that the efficiency in an induction heating device is improved as the overall electric conductivity

of the load decreases between certain limits. In this section, molten aluminium at 700°C, around 7.88 times more resistive than the previous solid aluminium, is taken for showing the second application involving susceptors. The worked example and results of K. Reichert (Reichert, 1965) are referred. There, a coreless induction furnace using a conductive crucible made out of graphite as a susceptor, is analysed for melting aluminium. Despite graphite is not that good conductor as molten aluminium is, the more resistive the load the more is enhanced the electromagnetic coupling. In Reichert's paper an analytical approach using Bessel functions is presented and confronted to field data measured in a real device
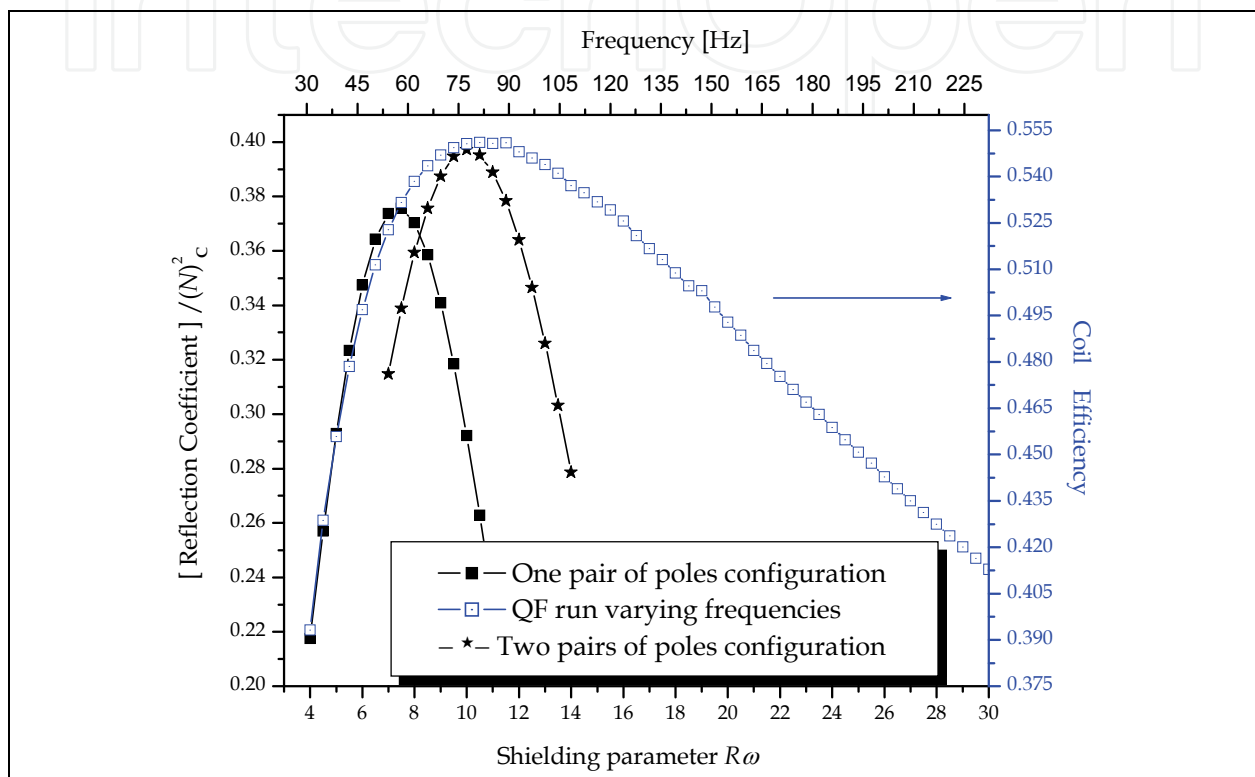
Fig. 7. Electromagnetic Coupling Parameter Performance in a Pole Paired Transverse Flux Scheme

In the following, besides of comparing his results on the coreless furnace features as far coil efficiency is concerned, further QF exercises are set up according to the various inductor configurations previously analyzed, now as a monolayer winding, and then corresponding coil efficiencies compared.

5.2 Reichert's assembling layout.

Table 3 shows the lay out and the electric conductivities of each component of the Reichert's assembling. 80 % of the total radius of the induced load corresponds to the molten pool and the remainder to the crucible thickness. Magnetic properties for magnetic yokes are not displayed in the worked example, therefore a typical non-linear magnetic permeability chart as shown in Fig. 9, is considered as corresponding QF input data. Also their electric conductivity was taken as null, in order to consider the insert/molten pool as only constituents of the induced resistive load in the QF simulation. Figs.10 and 11 show sketches for the layout of the Table 3. Details on coil cooling requirements are supposed to be already covered in Reichert's design, thus they are not discussed in this section.
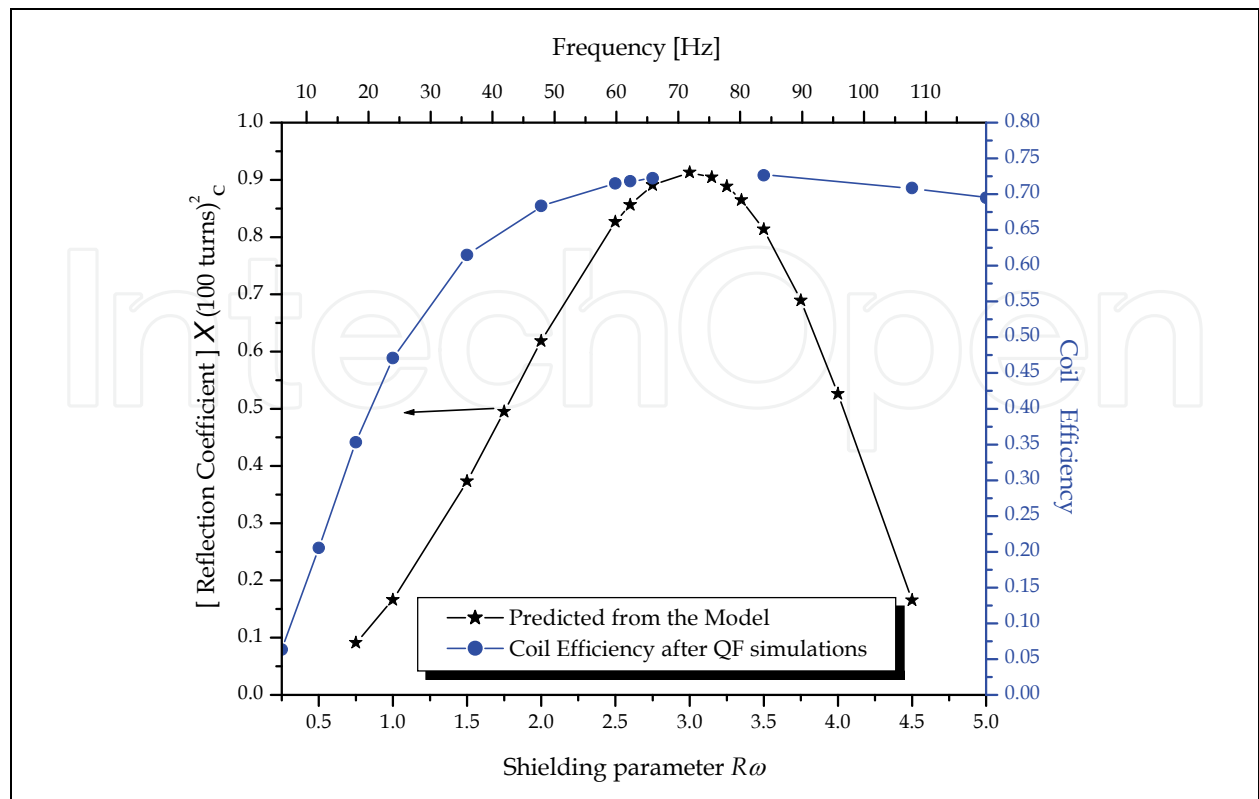
Fig. 8. Electromagnetic Coupling Parameter Performance in a Slab being excited by a Magnetic Transverse Flux.

Heigth = 0.51 m	Outer Radius [m]	Thickness [m]	Electric Conductivity [S m⁻¹]
Molten Aluminium	0.34	-	2 941 176
Graphite Crucible	0.425	0.085	166 666
Insulation Layer	0.475	0.05	0
Inductor Copper	0.492	0.017	55 556 000
Magnetic Shunts	0.52	0.028	0

Table 3. Lay out and electric conductivities for Reichert's assembling

5.3 Reichert's assembling coil efficiency featuring

When it comes to melting of metals at mains frequency, a crucible made out of a dense refractory has to contain the molten metal to stand mechanical erosion due to the strong stirring, which is driven by the induced Lorenz force. As a shortcoming, dense refractory has high thermal conductivity, which transfers heat to the excitation coil. Then a high porosity refractory is placed as thermal insulation layer in between to protect the coil copper and save energy. The addition of non-conductive regions to the gap between inductor and workpiece pays a penalty to the coil efficiency.

Table 4 shows the frequency and voltage supply, as being the input for both the worked example and QF exercises. As a result, coil efficiencies and fractions of the heat released to the total power in each component are also shown in the same Table. In the last row of Table 4, the basic features of a HI system where molten aluminium is performing only as a
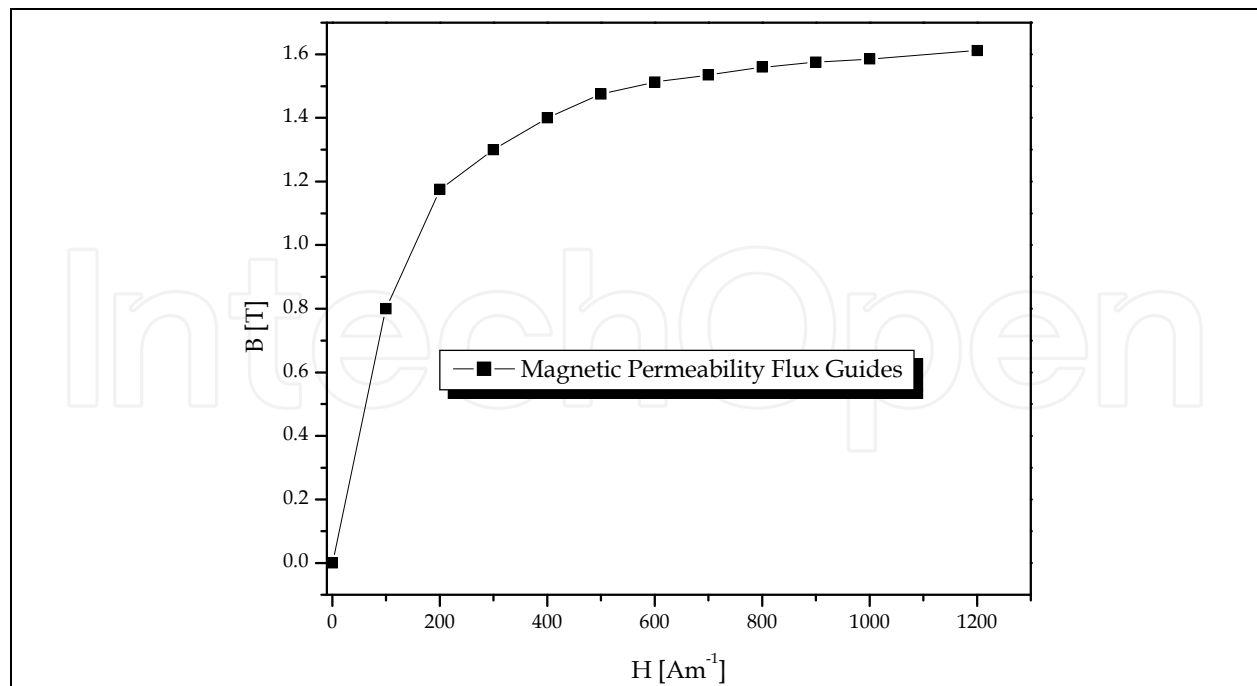
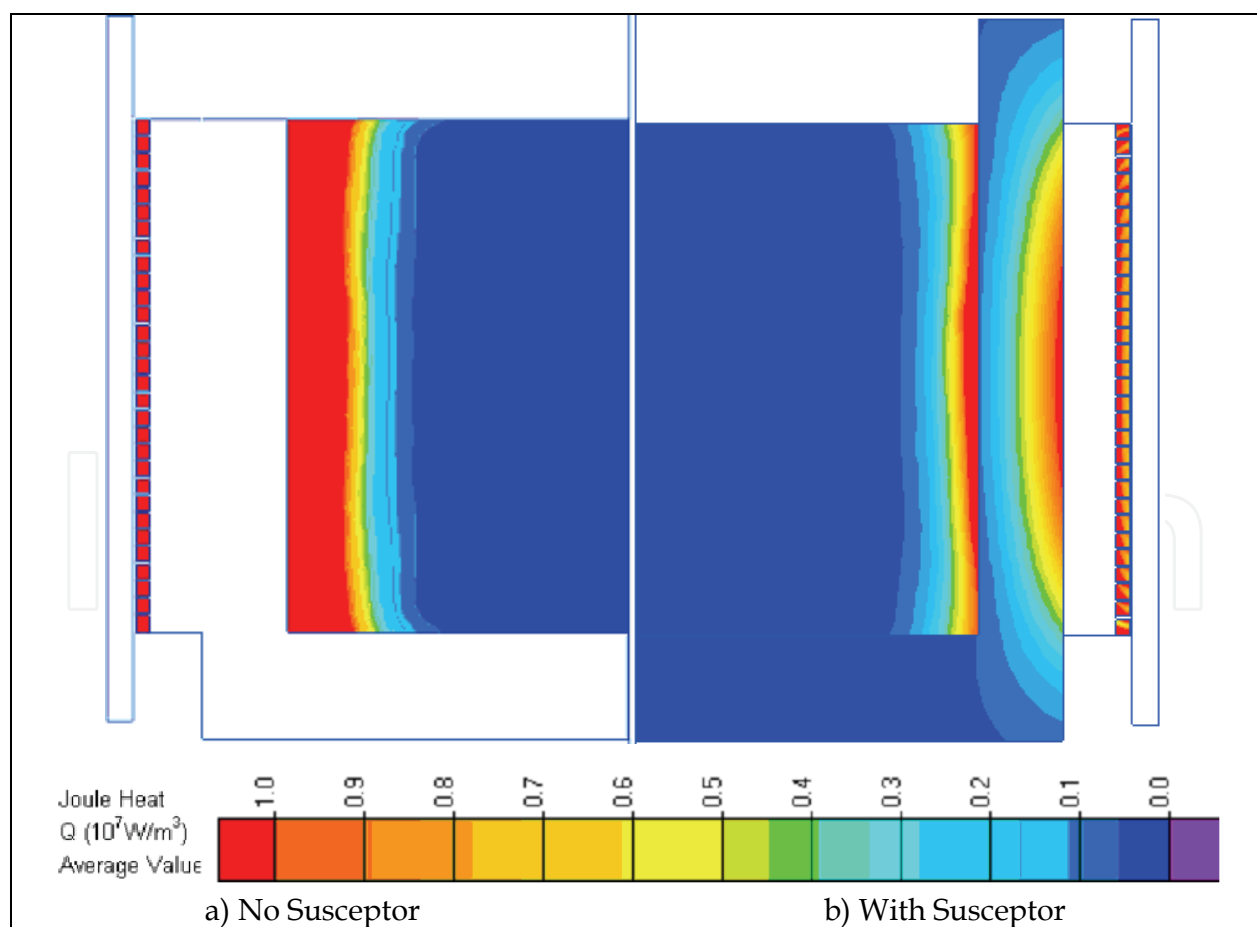Fig. 9. B vs H behaviour for the Magnetic Yokes in the Graphite-Aluminium assemblages

Fig. 10. Layout for a coreless induction furnace: a) Only Molten Aluminium as the workpiece b) Graphite Crucible and Molten Aluminium.

Supply: 380 V, 50 Hz Coil turns: 30	Current [A]	Rated Power [kW]	Susceptor Power Fraction	Molten Pool Power Fraction	Coil Efficiency
Field Data	1 640	134	-	-	-
Reichert's Model	1 690	125	0.39	0.33	0.72
QF run	1 670	137.73	0.4442	0.3406	0.7848
QF run*(Input: 391 V)	1 640	84.07	-	0.657	0.657

(*)Non-conductive Crucible

Table 4. Power Distribution in Reichert's Assemblage

workpiece is displayed. Here it is supposed that a dense crucible that contains molten aluminium is a non-electric conductor, thus the thickness of both the crucible and the insulation layer becomes an enlarged inductor-workpiece gap, which lowers coil efficiency. This layout is depicted in the left-hand-side of the Fig. 10. The corresponding Shielding parameter $R\omega$ is 134.23.

Coil efficiencies for $R\omega$ between 125 and 190 are obtained by means of QF runs, by taking into account same Inductor-Workpiece arrangement but varying frequency between 50 and 70 Hz. Those efficiencies are shown at the right-hand-side ordinate in Fig 3. Although the maximum difference in coil efficiencies displayed is 0.003, they resemble the rise and fall of the corresponding reflection coefficient curve. Both curves are bell-shaped and share approximately the same width. On the other hand, the peak of the reflection coefficient for the Fig.3 is 0.59427 whereas in Fig 2 is 0.337, hence the $R\omega$ region for the former might lead to a given HI layouts seemingly more robust as far as coil efficiency is concerned.

By fixing the same current as measured in the real device, 1640 [A] for the QF runs, the results show that both throughput and coil efficiency are the lowest for the molten aluminium by itself, as can be seen in last row of the Table 4. Once a crucible made out of dense graphite is placed instead of a non-conductive one, the efficiency (+19.45%) and the throughput of the assembling as well increase, according to rows 3 and 4 of Table 4. Deviations of QF results with respect to the field data of the Reichert´s assembling are: 2.78 % on rated power and 1.83 % on electric current which are close fair enough.

6. Proposals for new schemes of HI susceptor assemblies for improving coil efficiency

So far, this chapter has dealt with the finding of optimal configurations of HI systems regarding: size and shapes of inductors, application of either longitudinal or transverse excitation flux when appropriate and the use of susceptors in coreless furnaces (solenoidal scheme). All of these while keeping the lowest operational frequency, so as to avoid frequency converters or at least lowering eddy currents losses in the ancillary equipment.

In this section, combinations of the above schemes are analyzed, taking into account same materials, same frequency, similar both size and operational features, e.g. voltage and current as in the previous susceptor analysis.

6.1 Rectangular susceptor assembly excited by a transverse flux

In order to emulate the heating process that undergoes a slab under the effect of an excitation transverse flux on the previous HI susceptor schemes, a case is simulated below

with the QF software, considering molten aluminium contained in a box made out of dense graphite which in turn is surrounded by straight coils connected in series, resembling a rectangular cage. This particular coil design is known as "Ross "coil. The graphite box might be shifted out from one side of the monolayer coil cage for being either fed with raw materials or tilted for pouring out the melt. The thicknesses for the graphite walls and the back up insulation layer are the same as for the Reichert's assembly. The top view of the Ohmic losses spreading for this device is included in Fig 11 b). Coil efficiency and power distribution are shown in Table 5. Its performance looks better than the solenoidal assembly. Generally speaking, straight coils are easier to shape than circular ones. As a matter of fact, the real graphite "cylindrical" crucible as referred in Reichert's paper was actually an octagon 0.08 m thick, 0.51 m tall.

6.2 Cylindrical susceptor assembly excited by one-pair-of- poles transverse flux

Here the induced cylindrical load, which is comprised the dense graphite crucible, the inner molten pool, together with the outer insulation layer, have same dimensions and conductivities as in the Reichert's layout. The only thing that changes is the winding. Now this time straight coils run outside insulation layer parallel to the cylinder axis in each half of the cylinder, starting approximately at 90° arc apart each other so as to minimize the

a) Composite Cylinder   b) Composite rectangular Box
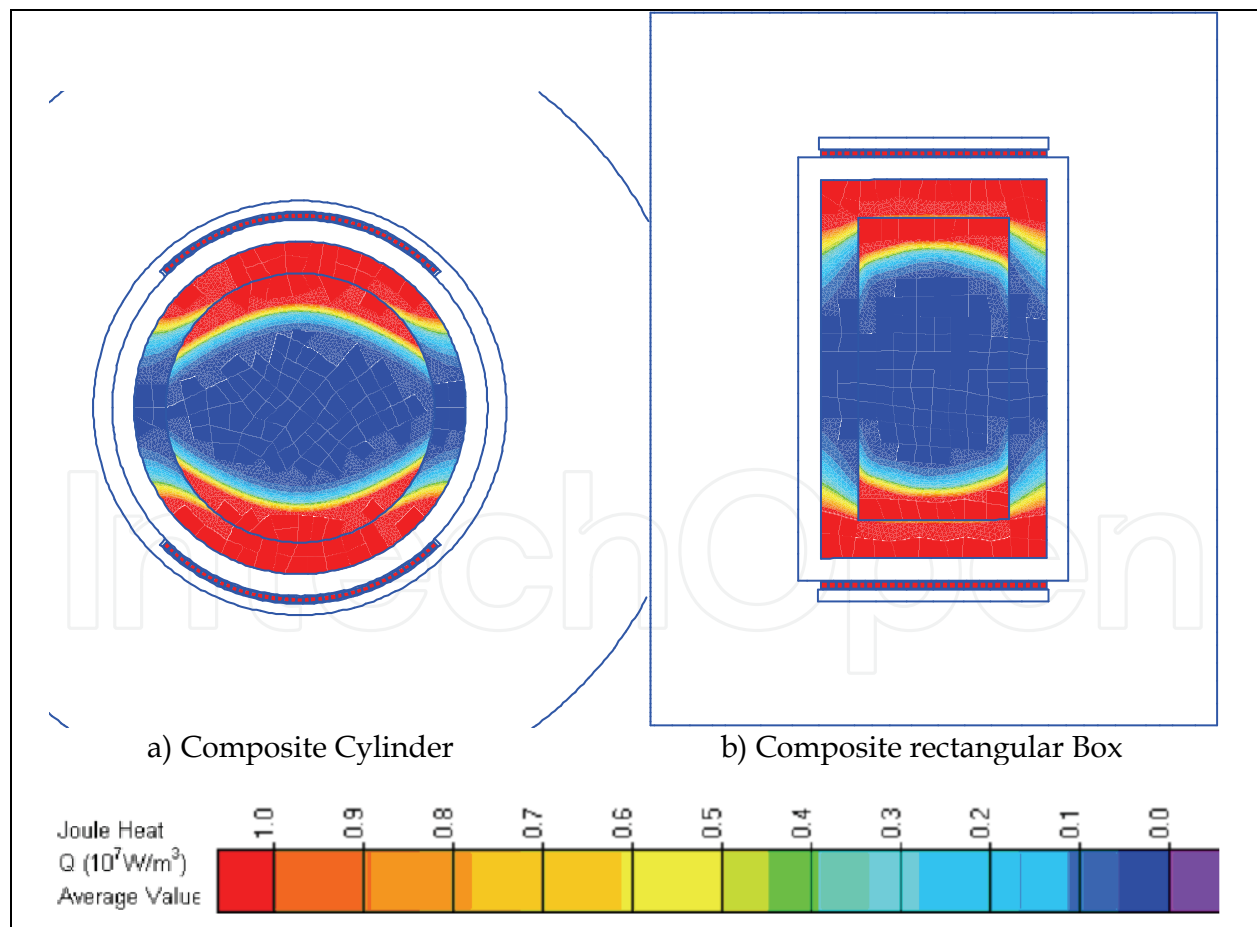
Joule Heat Q (10^7W/m^3) Average Value

Fig. 11. Top view of the QF simulations for the Joule Heat Distribution in a Composite Load being excited by a Transverse Flux

proximity effect between opposite windings. See the sketch in Fig 11 a). The ends of this single winding would connect as depicted in Fig. 12 where just one half of the straight winding is presented for purposes of clarity. Coil efficiency and power distribution are shown in Table 5. It seems this configuration is the most promising among those analysed in section 6. The heavy Joule heat dissipation located near to centres of each winding, as shown in Fig 11 a) would fade due to the vigorous stirring that occur in melting of metals at mains frequency.

Frequency: 50 Hz Height: 0.51 m	Current [A]	Rated Power [kW]	Susceptor Fraction	Molten Pool Fraction	Coil Efficiency
QF run (Reichert's Scheme] Supply: 380 V, Coil turns: 30	1 670	137.7	0.4442	0.3406	0.7848
Susceptor: Box Supply: 292 V Straight Coils: Top 30 /30 Bottom	1 652	66.96	0.537	0.3222	0.8592
One pair of poles Susceptor: Cylinder Supply: 274 V Straight Coils: Top 45 /45 Bottom	1 642	60.83	0.5935	0.3960	0.8842

Table 5. Power Distributions in New Schemes of HI Susceptor Assemblies.
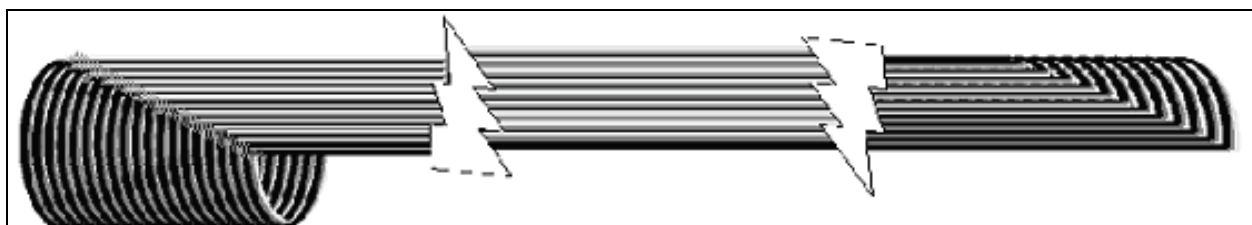
Fig. 12. Proposal for Connecting Coils at the Ends of the Device depicted in Fig. 11 a)

7. Conclusion

A mathematical model for obtaining a reflection coefficient for the workpiece contribution to the impedance of a given HI system was given. This is intended to asses how workpiece is linked to the excitation loop thus in order to find out conditions where the eddy current occurrence is enhanced, thus proving empirical rules already know for HI practitioners and to extrapolate those findings to design new possibilities. Quick Field Element Finite Sofware runs featuring coil efficiency of several HI systems were carried out so as to demonstrate the validity of the proposed approach. Calculated reflection coefficient shown rapid decay as long as the workpiece diameter to skin depth ratio goes beyond the optimum when comparing with coil efficiency. For simplification purposes, eddy currents process occurring inside the inductor itself have been neglected in this analytical approach. In the

future, taking into account eddy currents process occurring inside the inductor might predict the above slow decay in coil efficiency among others refinements to take. Nevertheless, this simplification enabled explanations of current practices in HI systems as well to set a generic guide for exploring new alternatives to those already known

8. References

Carrillo, E. (2008). Optimization of Electromagnetic Coupling in Induction Heating Systems Excited by Solenoidal and Axial Windings, *International Journal of Applied Electromagnetics and Mechanics*, 28, (3), 2008, pp. 395-412.

Krawczyk, A & Tegopoulos J. (1993). *Numerical Modeling of Eddy Currents*, Clarendon Press, Oxford, pp. 5, 6, 27.

Constantinides, A., (1987). *Applied Numerical Methods with Personal Computers*, McGraw-Hill, pp. 406–412, 418–439.

Black M., Cook R.., Loveless D., & Rudnev V. (2003) *Handbook of Induction Heating*, Marcel Dekker, New York, pp. 467, 527–528, 536–538, 599.

Davies, J. & Simpson, P. (1979). *Induction Heating Handbook*, McGraw-hill Book Company (UK) Limited, pp. 146,321,327.

 Harvey, I.G. (1977). A method of improving the energy transfer in induction heating processes and its application in a 1 MW billet heater, In: *IEE Conference Publication, 149*, Electricity for Materials Processing and Conservation, 1977, pp. 16–20.

Reichert, K. (1965). Die berechnung von kernelosen inductiontiegelöfen mit elektrisch eitenden Tiegel (zweischttiegelofen), *Archiv für Elektrotechnik*, Vol. 6, (1965) pp. 376-397.
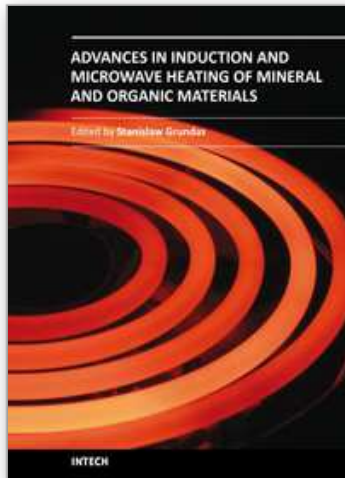
Advances in Induction and Microwave Heating of Mineral and Organic Materials

Edited by Prof. Stanisław Grundas

ISBN 978-953-307-522-8

Hard cover, 752 pages

Publisher InTech

Published online 14, February, 2011

Published in print edition February, 2011

The book offers comprehensive coverage of the broad range of scientific knowledge in the fields of advances in induction and microwave heating of mineral and organic materials. Beginning with industry application in many areas of practical application to mineral materials and ending with raw materials of agriculture origin the authors, specialists in different scientific area, present their results in the two sections: Section 1-Induction and Microwave Heating of Mineral Materials, and Section 2-Microwave Heating of Organic Materials.

INTECH
open science | open minds